J Solid State Electrochem (2010) 14:1997–2010
DOI 10.1007/s10008-010-1033-9

ORIGINAL PAPER

EXAFS structural studies of electrodeposited Co and Ni hexacyanoferrate films

A. Robert Hillman · Magdalena A. Skopek · Stephen J. Gurman

Received: 8 December 2009 / Revised: 10 February 2010 / Accepted: 10 February 2010 / Published online: 18 March 2010

Abstract XAS (EXAFS and XANES), XPS and IR spectroscopies were used to extract redox compositional and structural information on films of electrodeposited Co and Ni hexacyanoferrates whose redox state was manipulated electrochemically. The X-ray methods provided direct information on the metal species and IR provided indirect information via the behaviour of the ligand vibration. XPS responses showed that the electrochemical response of Co hexacyanoferrate is attributable to Co (except for a small amount of Fe^{II} oxidation at very positive potentials), and of Ni hexacyanoferrate to Fe; XANES edge shifts confirm these deductions. Local structure around the metal atoms was extracted from EXAFS data in terms of M′–N, M′–C and M′–Fe (M′ = Co or Ni) distances and the associated Debye-Waller factors as functions of film charge state. For Co hexacyanoferrate, the redox variation of static disorder was consistent with a molecular model involving discrete Co^{II} and Co^{III} sites, whose populations respond to potential, but not with a solid-state model.

Keywords EXAFS, XPS · Electroactive film · Hexacyanoferrate · Co · Ni

Introduction

Metal hexacyanometallates have attracted considerable attention in view of their interesting and potentially useful physical and chemical properties. While a major attraction is the facility to vary the metal ions present, the overwhelming majority of effort and insight relate to the Fe-based parent material, Prussian Blue. Here we focus on the structures and properties of two far less well-explored analogues in which the uncomplexed Fe is replaced by Co or Ni. Studies on this class of materials frequently involve samples that are prepared or manipulated chemically: this enhances their notorious variability of composition and properties with preparative and handling protocols. We use an electrochemical approach: this provides more convenient control over the conditions and thence more effective and precise control over redox composition of the material in thin film form. In order to address a number of controversial issues, we use XAS and XPS to identify the site of electroactivity, and XAS and IR spectroscopy to characterise the resultant structural changes. While these techniques have been used to study Prussian Blue type materials, their application has generally been distributed across samples whose similarity of composition could not be verified and whose redox state was not electrochemically established. Here, coordinated application of these techniques, in conjunction with electrochemical control of film charge state, reveals a coherent picture of Co and Ni hexacyanoferrates that highlights significant differences between the two of them along with distinctions from the parent Fe-based material.

Metal hexacyanometallates are mixed-valence complexes of composition $[A_xM'_yM''(CN)_6]\ zH_2O$, where M′ and M″ are divalent or trivalent transition metal ions and A is a univalent cation (most commonly Li^+, Na^+, K^+, or Cs^+). The univalent cations occupy interstitial sites in the lattice and their primary function is to maintain electroneutrality; this latter constraint determines their stoichiometry, represented by the value of x. The remaining interstitial volume may be occupied by water [1, 2].

A. R. Hillman (✉) · M. A. Skopek
Department of Chemistry, University of Leicester,
Leicester LE1 7RH, UK
e-mail: arh7@le.ac.uk

S. J. Gurman
Department of Physics and Astronomy, University of Leicester,
Leicester LE1 7RH, UK

The parent material with M′ = M″ = Fe is Prussian Blue (PB), whose existence (though not detailed composition or structure) has been known for around 300 years. While the literature of this family of materials is dominated by studies of PB itself, there are a number of reports of derivative materials. Indeed, the possibility to vary all three metals and the redox states of M′ and M″ are primary attractions. This provides scope for manipulation of material properties such as electrochromism and thermochromism [2, 3], ion-exchange [4–6], mixed-valence electrical conductivity, charge storage capabilities [7], and electrocatalytic [8], optical [9] and magnetic [9, 10] characteristics. The properties of metal hexacyanoferrates (M″ = Fe) can be also influenced by a range of external conditions such as temperature [9–11], illumination [9, 12, 13] or applied potential [9, 14]. This makes hexacyanometallates attractive for applications in a variety of (bio)sensors [15–21], batteries [22–24], separations [4, 6, 25, 26], optically switchable molecular compounds [9, 13], high-temperature molecular magnets [13, 27–29] and electrochromic devices [16, 30]. These materials has been studied as powders and pellets [31], as guests in various types of matrices [2] or as films in the context of modified electrodes [32], via polymer entrapment [33], adsorption [34] or electrodeposition [35] strategies.

The apparent simplicity of the synthesis and composition of PB and analogues is somewhat misleading. Relatively minor variations in deposition procedure, handling protocol, medium of exposure and redox history can lead to variations in structure or to significant departure from the simplistic formula given above. Materials prepared by chemical and electrochemical methods, but otherwise apparently similar, are known to be quite distinct. As a consequence, the literature contains many inconsistencies and ambiguities: this is true even for the much-studied parent PB system and the situation is more extreme for the derivative systems (such as the Co and Ni hexacyanoferrates studied here) upon which lesser effort has been expended. Nevertheless, careful selection of techniques can provide clarity and reveal structural complexity and subtlety, as demonstrated for the parent Prussian Blue [36] and derivatives involving substitution of Fe by Cd [37–39] or Cu [40].

The most common variations are associated with the interstitial sites, which tend to be filled with solvent molecules or with the counterions used in the synthesis. The water content may vary from sample to sample, and is very sensitive to the preparation and storage conditions [41, 42]. Solids may contain several phases with different chemical environments around the M′ sites, or bridging cyanide ligands may undergo linkage isomerism [42, 43]. The extent of linkage isomerism depends strongly on the electronic structure of M′ and M″; it does not occur at all in some PB analogues but is very common in others [42].

While electrochemical techniques are extremely effective in determining the extent and rate of electron transfer, they do not identify the source or sink of the electron(s). Thus, for example, there are conflicting reports in the literature about whether (or under which conditions) it is the Co or Fe that is the electroactive site when M′ = Co and M″ = Fe [2, 3, 11, 12, 14, 44]. The electrochemical behaviour of Co hexacyanoferrate appears to depend on the preparation route and on the nature of the interstitial countercation [2, 3]. Recent studies [1, 2] of Co hexacyanoferrate entrapped in a matrix comprising sol–gel-derived silica and generation 4 poly(amidoamine) dendrimer suggested that complex electrochemical processes involving more than one species are possible. Both metal sites have been proposed as redox centres and the additional possibility of metal-to-metal electron transfers (Fe^{III}–CN–Co^{II}⇌Fe^{II}–CN–Co^{III}) has been invoked. An additional argument [2, 10] is that the existence of Co^{3+} is associated with the "insoluble" form of hexacyanoferrates, as the lack of a $Fe(CN)_6$ unit gives more flexibility to the Co local environment, facilitating oxidation of the cobalt redox centre. On the basis of XPS and other spectroscopic observations, Sauter et al. [14] concluded that Co is the redox site in Co hexacyanoferrate, and that Fe is the redox site in Fe hexacyanoferrate. However, as discussed later, the *surface* sensitivity of XPS brings ambiguities in terms of *bulk* speciation; additionally, these measurements were made on films prepared differently to those studied here.

Photoinduced redox transformation of the low spin Co^{III} state to the high spin Co^{II} state has also been reported [14]. On the other hand, for Co hexacyanoferrate prepared by a precipitation route, Kulesza and co-workers suggest that Fe is the electroactive site in the presence of Li^+, Na^+, K^+, Cs^+ and Co^{2+} countercations [3], although in the presence of the last two of these cations the film is much less electroactive. In the presence of K^+ and Na^+ cations, a combination of Mössbauer, IR, UV-visible and EXAFS spectroscopies has been used to deduce that the redox chemistry of Co hexacyanoferrate (prepared by an electrochemical route, but not identical to that used here) is dependent on the electrolyte cation according to [9]:

NaCl solution :

$$Fe^{II} - CN - Co^{II-HS} \rightleftharpoons Fe^{III} - CN - Co^{II-HS}$$

KCl solution :

$$Fe^{II} - CN - Co^{II-HS} \rightleftharpoons Fe^{II} - CN - Co^{III-LS}$$

Lezna et al. [12] deduced complex relationships between different Co hexacyanoferrate samples on the basis of voltammetric, IR and XPS experiments. In the presence of

K^+ ions, XPS data clearly displayed a change in the Fe line but not the Co line, signalling Fe as the redox centre. Irradiation of the sample with near IR radiation was also reported to generate the $Co^{III}Fe^{III}$ compound. EXAFS data reported by Yokoyama et al. [10] for chemically and electrochemically prepared Co hexacyanoferrate films as a function of temperature showed a change of Co oxidation state from Co^{III} at 30 K to Co^{II} (with some residual Co^{III}) at 296 K. For Ni hexacyanoferrate, an interesting contribution has been the comparison of XRD and EXAFS to explore structure and structural order on different length scales [45].

The general objective was to determine the equilibrium compositions and local structures around the metal species within electrochemically deposited and redox-manipulated Co and Ni hexacyanoferrate films. The (non-)variations of bond lengths, coordination numbers and Debye-Waller factors with applied potential are then to be used to assign chemical identities to the species associated with changing film charge state, i.e., to identify the sources and sinks of electronic charge.

As will be clear from the foregoing summary of the literature, the primary novelty of the present study is the coordinated use of EXAFS and supporting spectroscopic techniques on electrochemically prepared Co and Ni hexacyanoferrate films whose charge was systematically manipulated across a range of partially and completely converted redox states. While a substantial body of literature exists for characterization of electrodes modified with Prussian Blue and its analogues, and there are EXAFS studies involving *chemically* prepared pellets of the Co and Ni analogues [44], these are not compositionally or structurally the same as *electrochemically* prepared material. The significance of the present study is that comparisons between the outcomes of the various methods can be made with confidence that the samples are synthetically and redox history identical; the evidence (above) is that this has been a limiting factor to progress in understanding these systems, as exemplified by the differing conclusions regarding Co or Fe as the electroactive site in cobalt hexacyanoferrate [3, 44].

Experimental

Materials

Co and Ni hexacyanoferrate films were deposited from de-oxygenated (N_2 or Ar purged for 30 min) aqueous solution comprising 25 ml of 0.5 M potassium chloride (Fisher Scientific) and 50 μl of either 0.5 M cobalt(II) chloride hexahydrate (Riedel-de Haën) or 0.5 M nickel(II) chloride hexahydrate (Fluka) to which was added 50 μl of de-oxygenated 0.25 M potassium ferricyanide (Sigma-Aldrich).

Instrumentation

Electrochemical measurements were made in a conventional three-electrode cell, using an ECO CHEMIE μAutolab PGSTAT 20 potentiostat under computer control. The working electrode was a Pt disc (EXAFS) or ITO-coated glass (XPS and FTIR), the counter electrode was a large area Pt gauze and the reference electrode was either a saturated calomel electrode (SCE; for the EXAFS and XPS samples) or Ag/AgCl/sat'd KCl (for the FTIR samples).

X-ray measurements were made at the synchrotron radiation source (SRS, Daresbury Laboratory, UK). EXAFS spectra were taken ex situ in fluorescence mode on beamline 16.5 (30-element solid-state Ge(111) detector) or beamline 7.1 (nine-element Si(111) detector). Measurements were taken at the Fe K-edge (7,125 eV), Ni K-edge (8,333 eV) and Co K-edge (7,710 eV) up to $k_{max}=14$ Å^{-1}. Typical acquisition times were 30–40 min. XPS measurements were made using monochromatic Al Kα radiation (E=1,486.7 eV) on the Scienta ESCA300 spectrometer at the National Centre for Electron Spectroscopy and Surface Analysis at Daresbury Laboratory. The take-off angle was 90°. An electron flood gun was used to prevent sample charging. IR data were recorded ex situ in transmission mode (Perkin Elmer Instruments Spectrum One FTIR spectrometer).

Procedures

Films for electrochemical and spectroscopic characterization were made using identical procedures: potentiodynamic cycling from 0.0 V to +0.9 V (SCE) at a scan rate, v= 0.1 V s^{-1}. Where the experiment or exploration of parameters demanded, film thickness was varied via the number of deposition cycles, typically varied in multiples of 50 cycles. Films for XAS, XPS and FTIR spectroscopy were deposited by 150, 50 and 50 redox cycles. Freshly deposited films were cycled ten times in 0.5 M KCl electrolyte at scan rate, v=0.1 V s^{-1}, held for 20 min at the required potential, then removed from solution and rinsed with de-oxygenated deionised water prior to spectroscopic characterization at room temperature.

Spectroscopic data analysis

Fluorescence EXAFS spectra were summed, calibrated and background subtracted using the Daresbury programmes EXCALIB [46] and EXBACK [46]. Fitting was achieved using EXCURV98 [47], providing interatomic distances (R), coordination numbers (N), root mean square deviation of bond length (i.e., r.m.s. disorder or Debye-Waller factor, σ^2) and the elemental identities of neighbouring atoms. An estimate of uncertainties in the fitted parameters is also provided by the EXCURV98 fitting programme.

The electroactive surface population of sites (Γ/mol cm^{-2}) was calculated by integration of slow scan voltammetric responses to yield the charge (Q/C) and application of Faraday's law:

$$\Gamma = \mathrm{Q}/\mathrm{nFA} \quad (1)$$

where the number of electrons transferred per redox site, $n=1$, and A is the electrode area. An estimate of film thickness (h) was made assuming the film is predominantly hexacyanometallate, i.e., the volume fraction of electrolyte is small [48, 49]:

$$h = \frac{Q}{nFA} \cdot \frac{d^3 N_A}{4} \quad (2)$$

where d (cm) is the length of the unit cell, N_A is the Avogadro constant and the factor of four arises because there are four electroactive metal sites in the unit cell. For Co and Ni hexacyanoferrates, the length of the unit cell, $d=10.35$ Å [50]; this is slightly larger than for the parent Prussian Blue material [48].

Signal-to-noise constraints allowed EXAFS data to be fitted only up to $k_{max}=10$ Å^{-1}. For the Co K-edge in the Co hexacyanoferrate system, the first Co–N shell was fitted first and subsequent shells fitted stepwise, with progressive and significant improvement of the fit index. Although the [···Co–N≡C–Fe···] atom sequence is almost linear, inclusion of multiple scattering did not improve the fit. When the possibility of multiple scattering was included, the bond angles iterated to a point where this was not a significant effect; consequently, multiple scattering was not included in the fits.

There was a small shift between EXAFS data acquired at the two experimental stations (7.1 and 16.5) due to the monochromator calibration. To remove this systematic effect, all data are placed on a single scale, referred to the 7.1 calibration.

Results

Electrochemical responses

Cyclic voltammograms at a range of scan rates for representative Co and Ni hexacyanoferrate films are shown in Figs. 1 and 2, respectively. For the collection of films studied, film thicknesses (calculated as described above) were in the range 10–70 nm. The mean of the anodic and cathodic peak potentials at slow scan rates (where kinetic and transport limitations are minimised) was 0.56 V (vs. SCE) for Co hexacyanoferrate and 0.61 V (vs. SCE) for Ni hexacyanoferrate. The variations of anodic and cathodic peak currents with potential scan rate for both films was linear (see insets to Figs. 1 and 2). This signals that, within the range of conditions employed, there is complete redox conversion of the electroactive sites; this validates the coulometric assay represented by Eq. 1.

Extended X-ray absorption fine structure

k^3-weighted EXAFS data and the corresponding Fourier transform (radial structure function) acquired at the Co K-edge for a Co hexacyanometallate modified electrode are presented in Fig. 3. There are three clear peaks visible in the FT plot at distances of ca. 2, 3 and 5 Å, corresponding to distances from the Co atom to its neighbouring N, C and Fe atoms, respectively. Comparison of the experimental data and the fits shows that the precision is excellent for the nearest neighbours, but less good for the more distant (third shell) Fe atom.

XANES data at the Co K-edge as a function of Co hexacyanometallate film emersion potential, shown in Fig. 4, reveal obvious changes in position and shape. The former signals Co oxidation state changes. The significant characteristic of the latter is that the peak at intermediate potentials (partial redox conversion) is broad and has two components. As will be argued below in conjunction with Debye-Waller factor values, this is characteristic of a "molecular" rather than solid-state model, i.e., with localised sites of discrete oxidation state.

For the Co hexacyanoferrate films, full oxidation causes a shortening of the Co–N bond distances from 2.03±0.02 Å to 1.89±0.02 Å. The situation at intermediate potentials is more complicated. Fitting to a (hypothetical) single type of site results in a large Debye-Waller factor, indicating (at least) two types of site of distinct charge and geometry. Fitting to a two-site model results in lower Debye-Waller factors, more in line with those for the fully oxidised and fully reduced films; we interpret this to signal a mixture of oxidised and reduced Co sites, each with distinct geometry. There is also shortening of the Co–C and Co–Fe bond lengths. However, these do not (within experimental uncertainty) exceed the shortening of the Co–C bond lengths, so we interpret this to indicate that the N ≡ C unit and the Fe shift without internal change towards the Co atom.

The reproducibility of the data acquired on different instruments for different films (see Table 1) allows us to explore some more subtle features. Even at the extremes of potential, where the voltammogram indicates no further charge transfer, the Debye-Waller factors are higher than for the standard compound ($CoCl_2$), and suggest the presence of more than one Co–N distance. There are two possible sources of such an effect. The first is an electrochemical one, namely that the much thicker films (cf. Fig. 1) required for EXAFS experiments have morphology and/or transport

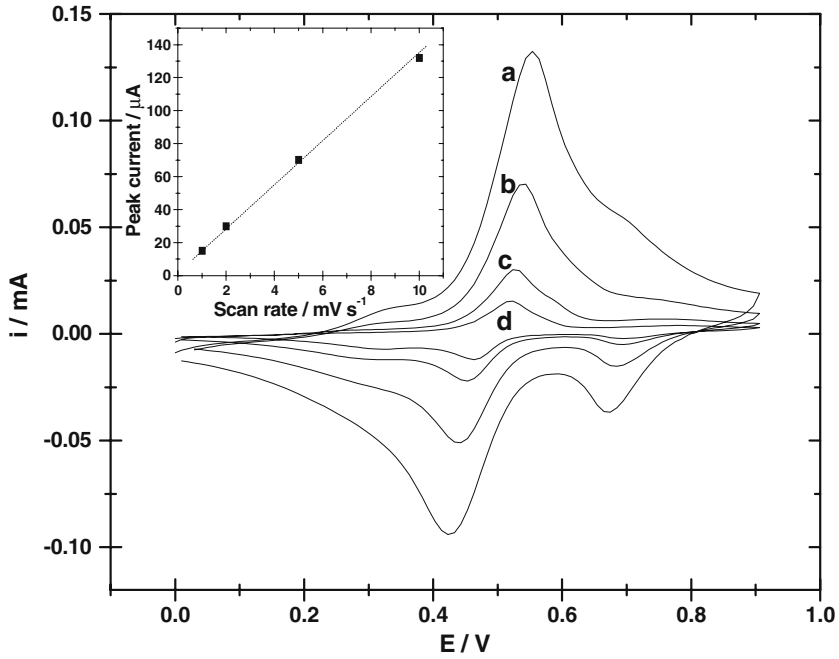

Fig. 1 Representative cyclic voltammograms of a cobalt hexacyanoferrate modified electrode in 0.5 M KCl. $\Gamma = 2.7 \times 10^{-8}$ mol cm^{-2} (thickness ca. 45 nm). Scan rates: (*a*) 10, (*b*) 5, (*c*) 2 and (*d*) 1 mV s^{-1}. *Inset* variation of anodic peak current with scan rate

characteristics that result in incomplete redox conversion, i.e., there is residual Co^{2+} (Co^{3+}) even at the most positive (negative) potentials. The second explanation is a compositional one, namely that the electrodeposition process may result in some interstitial cobalt (as a charge balancing ion, along with K^+). The standard redox potential of the $Co^{3+/2+}$ process in aqueous solution is +1.92 V vs. NHE [51], making it electrochemically "silent" and distinct from the electroactive Co sites that dominate film response. These interstitial cobalt counterions introduce additional disorder to the data, which is reflected in increased Debye-Waller factors. XPS data (see below) provide additional support for the latter effect.

The discussion of the Ni K-edge data in Ni hexacyanoferrate films (see Table 2) is brief, but diagnostically clear. XANES data at the Ni K-edge for Ni hexacyanoferrate films (exemplified by Fig. 5) are quite different, in that there is no significant variation in the white line position or shape. Analysis of the k^3-weighted EXAFS spectra and Fourier transform (see Fig. 6) reveal no significant change

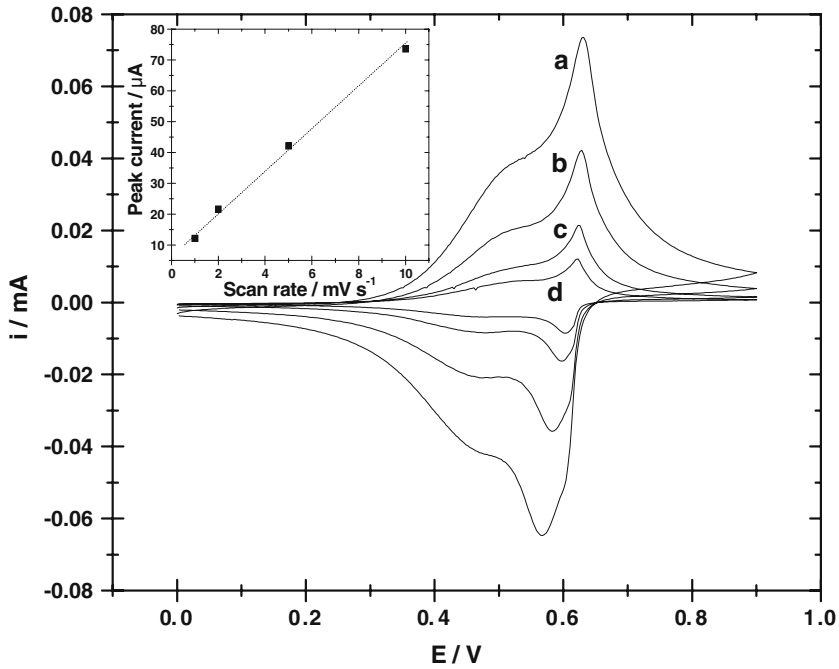

Fig. 2 Representative cyclic voltammograms of a nickel hexacyanoferrate modified electrode in 0.5 M KCl. $\Gamma = 6.8 \times 10^{-9}$ mol cm^{-2} (thickness ca. 12 nm). Scan rates: (*a*) 10, (*b*) 5, (*c*) 2 and (*d*) 1 mV s^{-1}. *Inset* variation of anodic peak current with scan rate

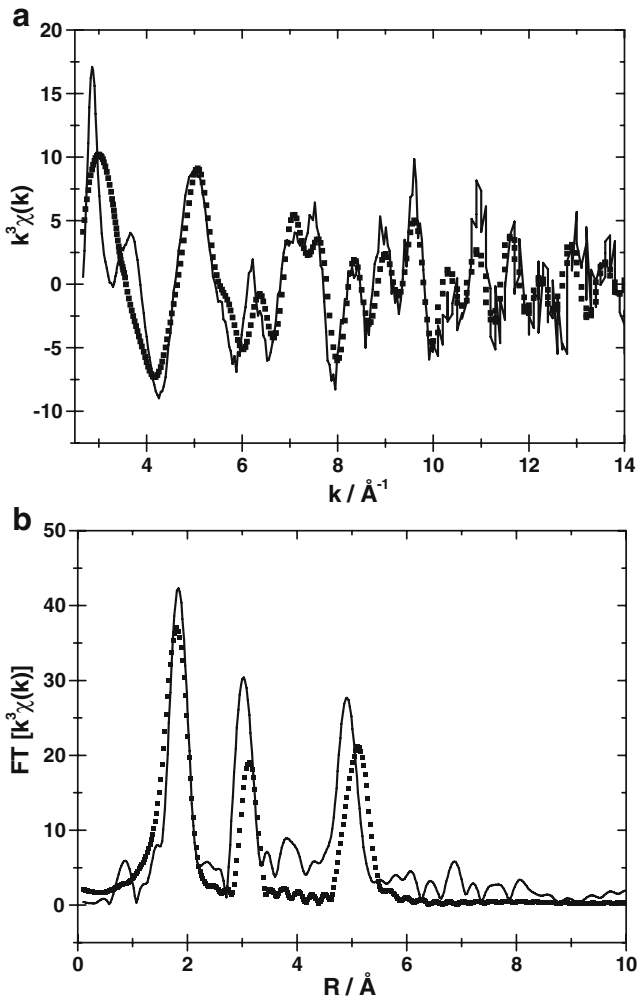

Fig. 3 **a** Co K-edge k^3-weighted EXAFS spectra of cobalt hexacyanoferrate film emersed at 0.9 V. **b** Fourier transform of data in (**a**); *line* experimental data, *points* fitted theoretical data

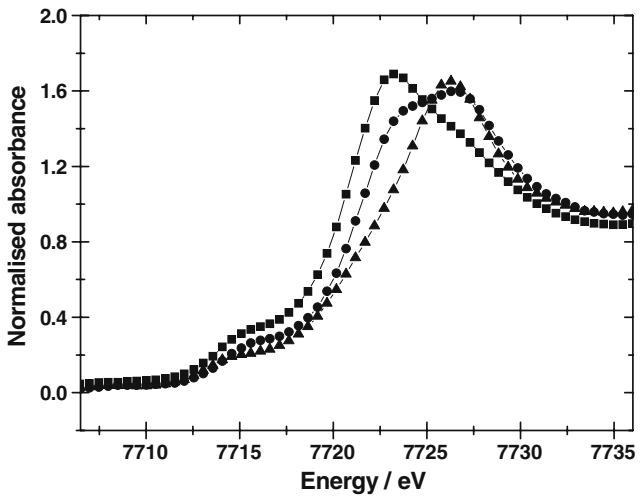

Fig. 4 XANES of the Co K-edge for a cobalt hexacyanoferrate film. Potential, 0.0 V *filled square*, 0.3 V *filled circle*, 0.9 V *filled triangle*

in the Ni–N, Ni–C or Ni–Fe distance between fully oxidised and fully reduced films. The qualitative implication is that the Ni centres are not the site of electroactivity in this potential range.

X-ray photoelectron spectroscopy

Figure 7 shows XPS data in the Co $2p_{3/2}$ and Fe $2p_{3/2}$ regions for a Co hexacyanoferrate film. Qualitatively, the observation is that the oxidation state of (some of) the Co responds to potential but, aside from a very minor effect at the most positive potentials, that of Fe does not. Similarly, Fig. 8 shows Ni $2p_{3/2}$ and Fe $2p_{3/2}$ spectra for a Ni hexacyanoferrate film. In this case, it is the oxidation state of Fe that responds to potential, with all the Ni remaining in the formal 2+ oxidation state. Quantitation of these population changes in Co (for Co hexacyanoferrate) and Fe (for Ni hexacyanoferrate) oxidation states is less simple. In the former case, both Co^{2+} and Co^{3+} are observed at all potentials, with the predominant species shifting from Co^{2+} to Co^{3+} with increasing potential. In the latter case, there is exclusively Fe^{2+} at the negative extreme of the potential range used, and predominantly (but not exclusively) Fe^{3+} at the positive extreme. The situation here is complicated by the fact that the transfer of the sample to the XPS UHV chamber necessarily involves exposure to the laboratory atmosphere, which is likely to influence the redox composition of the outer region of the film. Since XPS is surface selective, it samples only the region that is vulnerable to this redox "contamination". We therefore take the XPS data to be a source of unequivocal qualitative confirmation of the site of electroactivity, but not a quantitative measure of redox composition.

Integration of the relevant peak(s), taking into account elemental cross-sections, allows estimation of the relative populations of the elements present in the surface region of each film. Tables 3 and 4, respectively, show ratios of the elements present (irrespective of oxidation state) at the surfaces of Co hexacyanoferrate and Ni hexacyanoferrate films. Given the universal problem of surface contamination by carbon-containing species, we restrict our attention to the metals present and nitrogen (as an unambiguous marker for the ligand).

Simplistically, if the ideal film compositions (see above) applied, the Fe–Co and Fe–Ni ratios would be unity and the N–Fe ratio would be 6 at all potentials and the Fe–K ratio would decrease upon film oxidation. In all cases, we find the Fe–Co and Fe–Ni ratios low, i.e., there is excess Co or Ni. This is the result of some of the role of charge balancing counter ion being taken by interstitial Co or Ni; the presence of these (electroinactive) species was inferred from the EXAFS data (see above). The N–Fe ratios are a little high, but qualitatively reasonable. The Fe–K ratio is

Table 1 Structural parameters for Co hexacyanoferrate films at different oxidation states

Sample	Edge	Element	Distance, R/Å	Coordination number (N)	σ^2/(pm)^2
50 mM $CoCl_2$	Co K-edge	O	2.09±0.02	6±0.5	50±10
CoHCF film	Co K-edge				
0.9 V		N	1.89±0.02	6	130±60
		C	3.15±0.02	6	−25±10
		Fe	5.05±0.02	6	50±25
0.7 V		N	1.88±0.04	6	130±20
		C	3.18±0.02	6	40±30
		Fe	5.07±0.04	6	40±10
0.3 V single first shell		N	1.96±0.02	6	270±40
		C	3.27±0.02	6	50±30
		Fe	5.16±0.04	6	120±50
0.3 V split first shell		N	1.85±0.06	–	180±120
		N	2.04±0.06	–	190±160
		C	3.27±0.02	–	50±30
		Fe	5.16±0.04	–	120±50
0.0 V		N	2.02±0.02	6	220±50
		C	3.33±0.02	6	30±30
		Fe	5.16±0.08	6	140±100
Replicate		N	2.04±0.02	6	170±30
		C	3.35±0.02	6	60±30
		Fe	5.11±0.04	6	110±40
0.0 V	Fe K-edge	C	1.98±0.02	6	100±20
		N	3.13±0.03	6	80±50
		Co	5.21±0.04	6	90±40

Fits to EXAFS data truncated at k_{max}=10 Å^{-1}

not straightforward to interpret since some of the role of K^+ as a charge balancing ion is assumed by Co or Ni. However, it is clear that film oxidation, i.e., removal of electronic charge, is accompanied by ejection of K^+ to maintain electroneutrality, as manifested by the increase in Fe–K ratio. It is worth noting that the much larger variation with potential of the Fe–K ratio than Fe–Co or Fe–Ni ratio (in the respective cases) indicates that K^+ transfer is more facile than Co^{2+} or Ni^{2+} transfer; electrostatic arguments would seem to provide an explanation for this.

Infrared spectroscopy

Figure 9 shows IR transmission spectra for the ν(CN) vibrational bands of Co hexacyanoferrate films. Based on data for chemically prepared materials [52], the bands at

Table 2 Structural parameters for Ni hexacyanoferrate films at different oxidation states

Sample	Edge	Element	Distance, R/Å	Coordination number, N	σ^2/(pm)^2
500 mM $NiCl_2$	Ni K-edge	O	2.06±0.02	4.8±0.5	75±10
Ni hexacyanoferrate	Ni K-edge				
0.9 V		N	2.06±0.02	6	70±15
		C	3.33±0.03	6	40±30
		Fe	5.24±0.02	6	60±20
0.0 V		N	2.05±0.02	6	80±15
		C	3.33±0.02	6	40±20
		Fe	5.22±0.03	6	100±30
0.0 V	Fe K-edge	C	2.01±0.01	6	40±15
		N	3.26±0.03	6	15±25
		Ni	5.17±0.04	6	80±40

Fits to EXAFS data truncated at k_{max}=10 Å^{-1}

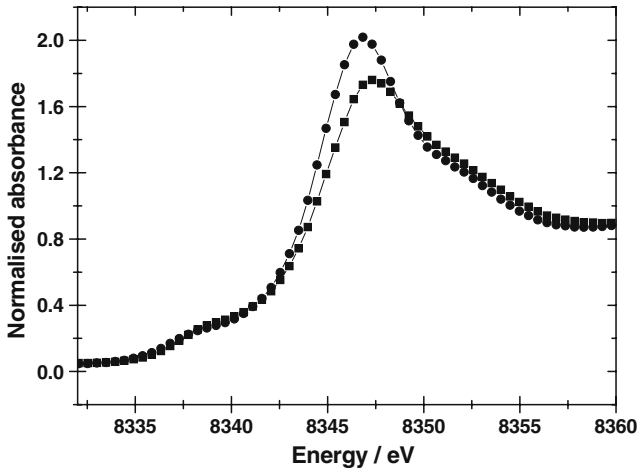

Fig. 5 XANES of the Ni K-edge for a nickel hexacyanoferrate film. Potential, 0.0 V *filled square*, 0.9 V *filled circle*

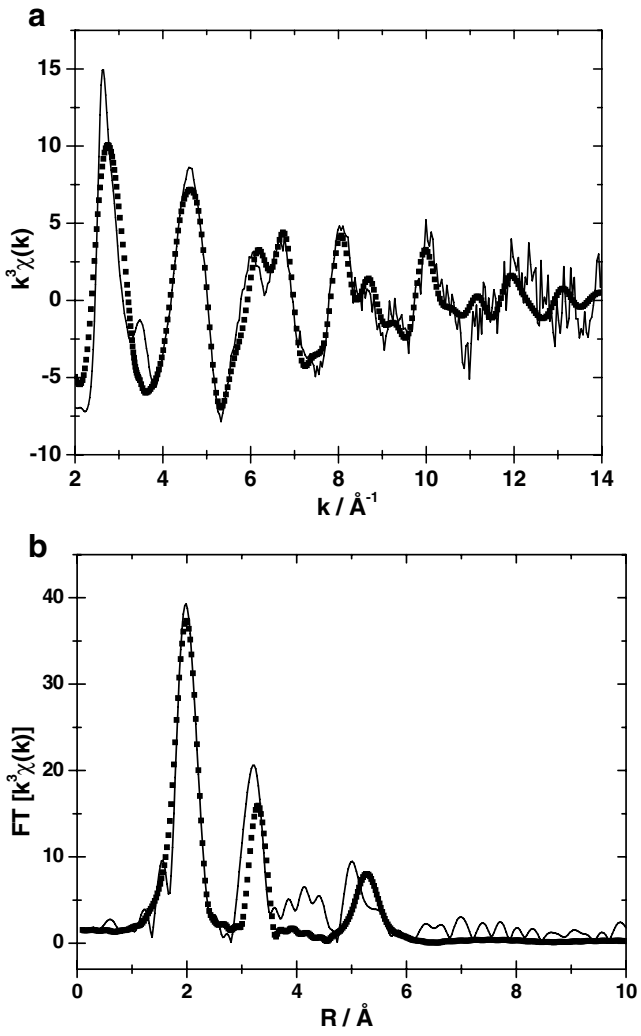

Fig. 6 **a** Ni K-edge k^3-weighted EXAFS spectra of nickel hexacyanoferrate film emersed at 0.0 V. **b** Fourier transform of data in (**a**); *line* experimental data, *points* fitted theoretical data

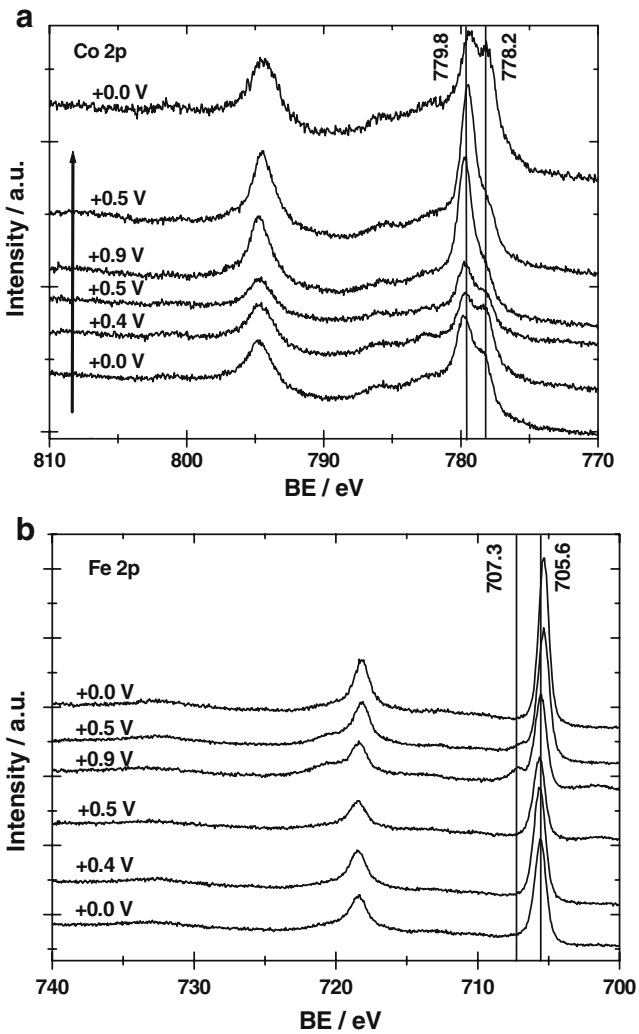

Fig. 7 **a** Co 2p and **b** Fe 2p spectra for a cobalt hexacyanoferrate film emersed at different potentials (as indicated); *arrow* indicates sequence of measurements. *Vertical lines* are a guide to the eye to assist in identifying (absence of) changes in peak position

2,099, 2,141 and 2,200 cm^{-1} can be assigned to $Fe^{II}Co^{II}$, $Fe^{II}Co^{II}Co^{III}$ and $Fe^{III}Fe^{II}Co^{III}Co^{II}$, respectively, where the nomenclature simply indicates the oxidation state(s) of the metals present. The potential variations of the strength of these bands indicates that not all the Co^{II} species are oxidised, as discussed above and commented on by Sauter et al. [14]. The feature signalling the presence of Fe^{III} is rather small, consistent with the earlier observation of this as a minority species in the XPS data.

The case of Ni hexacyanoferrate, illustrated by the ν(CN) vibrational band region IR transmission spectra in Fig. 10, is somewhat simpler. Assignment of the vibrational bands at 2,106 and 2,141 cm^{-1} to $Fe^{II}Ni^{II}$ and $Fe^{III}Ni^{II}$, respectively, confirms the X-ray spectroscopic-based deduction of no electroactive component from the Ni sites and a potential-driven shift from all Fe^{II} to dominant Fe^{III}.

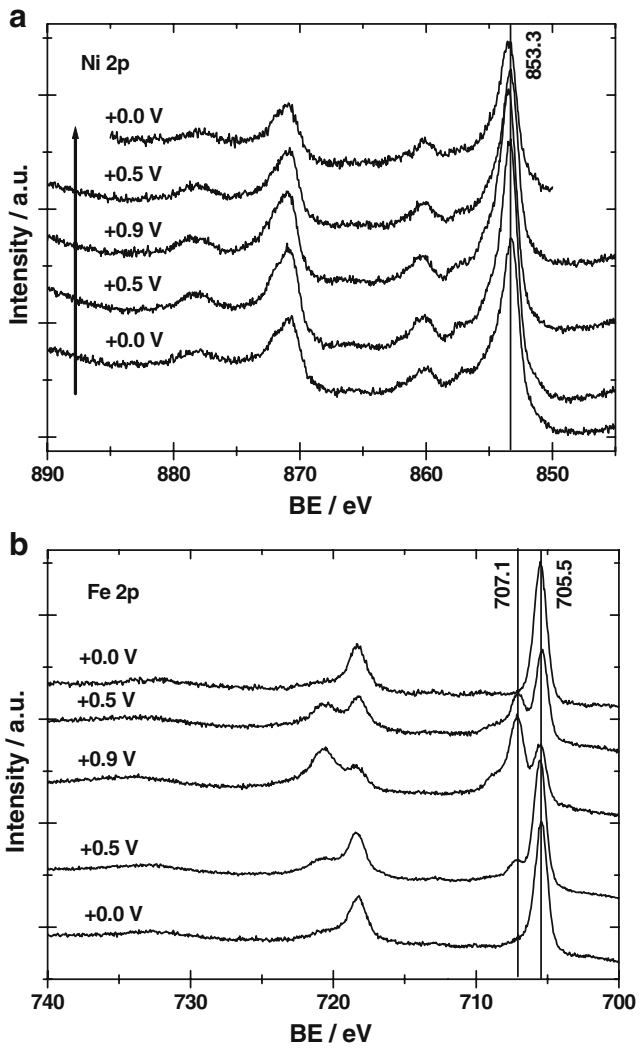

Fig. 8 **a** Ni 2p and **b** Fe 2p spectra for a nickel hexacyanoferrate film emersed at different potentials (as indicated); *arrow* indicates sequence of measurements. *Vertical lines* are a guide to the eye to assist in identifying (absence of) changes in peak position

In both systems, the increase in ν(CN) frequency (wavenumber) upon film oxidation is a consequence of the more positively charged metal ion withdrawing electron density from the N≡C bond. The fact that the vibrational bands undergo a blue shift indicates that the N≡C bond is stronger; this is consistent with removal of electron density from a π* orbital.

Table 3 Selected surface atom ratios (derived from XPS) for Co hexacyanoferrate films as a function of emersion potential

Potential	Fe/Co	Fe/K	N/Fe
0.0 V	0.6	0.6	8
0.4 V	0.7	0.5	7
0.5 V	0.8	0.5	8
0.9 V	0.6	1.0	8
0.5 V	0.7	0.8	7

Table 4 Selected surface atom ratios (derived from XPS) for Ni hexacyanoferrate films as a function of emersion potential

Potential	Fe/Ni	Fe/K	N/Fe
0.0 V	0.8	0.5	7
0.5 V	0.8	0.5	6
0.9 V	0.8	1.3	6
0.5 V	0.8	0.6	7

Discussion

Since the EXAFS data are the primary source of information, we begin with these. Of the two systems, the behaviour of Ni hexacyanoferrate is the simpler, so we discuss this case first. The Ni pre-edge structure is very similar to that at the Fe K-edge and shows no significant change in position with potential. The EXAFS data yield three shells; none of the distances associated with these shells changes with film redox state. In considering the relatively constant Fe···Ni distance, there are two factors worth noting. First, it is noticeable that the Fe–C distance changes little; this would be the main generator of a change in Fe···Ni distance. Second, the distances from the Ni, combined with a Fe–C distance of about 2.0 Å from the fitting of EXAFS data at the Fe K-edge, imply a non-linear [···Ni–N ≡ C–Fe···] arrangement, although the angles are all close to 180°. Variations in these small deviations from

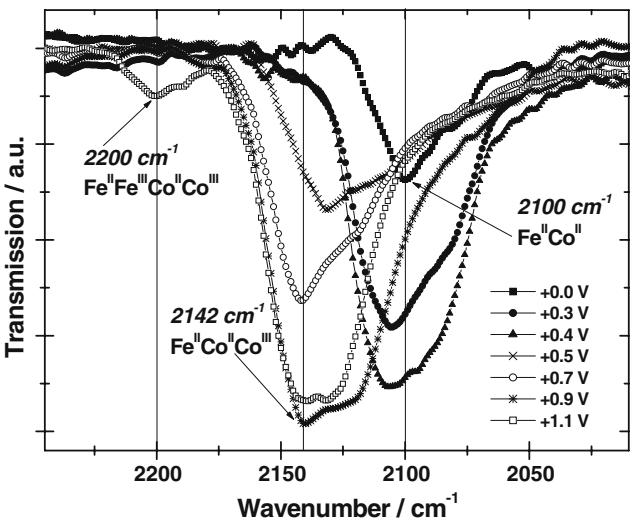

Fig. 9 FTIR transmission spectra in the ν(CN) region for a cobalt hexacyanoferrate modified electrode as a function of potential (as indicated). With film oxidation, ν(CN) increases from 2,099 cm^{-1} through 2,141 cm^{-1} to 2,200 cm^{-1}

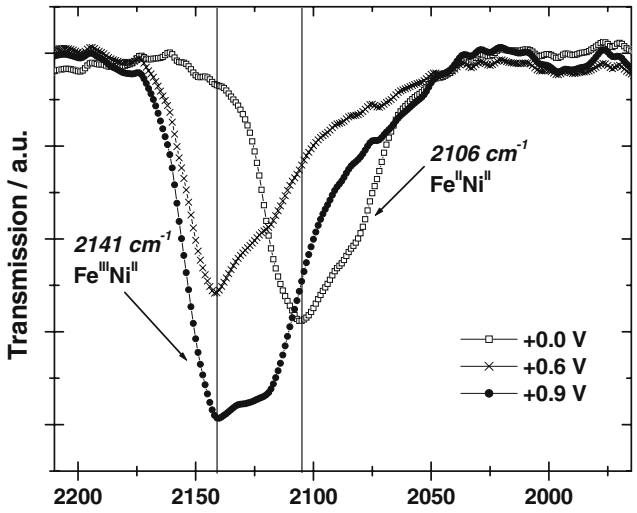

Fig. 10 FTIR transmission spectra in the ν(CN) region for a nickel hexacyanoferrate-modified electrode as a function of potential (as indicated). With film oxidation, ν(CN) increases from 2,106 to 2,141 cm^{-1}

linearity could also explain the constancy of metal–metal distance. Since the Ni is not electroactive, i.e., remains in the Ni^{II} state, there is no indication of a split first shell; this contrasts with Co hexacyanoferrate. The low values of Debye-Waller factors (σ^2) for the second and third shells suggest some multiple scattering, but not to the extent that it could be reliably fitted.

For the Co K-edge in the XANES of Co hexacyanoferrate films there is a marked increase in energy of the white line position as the film is oxidised. Before discussing this in detail it is worth recalling that the XAS data represent an average of *all* the film, which contrasts with the high (ca. nm) surface selectivity of the XPS data. At an emersion potential of 0.0 V, the energy of the white line (at 7,723 eV) is essentially the same as for Co^{2+} in aqueous $CoCl_2$. Increasing the emersion potential to 0.3 V, there is a clear doublet (at energies of 7,723 and 7,726 eV). This represents oxidation of some of the Co^{2+} sites to Co^{3+}; the peak intensities indicate a slight preponderance of Co^{3+}. At emersion potentials of 0.7 and 0.9 V, there is a single peak at 7,726 eV, signalling that conversion to Co^{3+} is essentially complete. At this point, we note that the static nature of the study prevents any investigation of mechanism—we simply detect Co(III) as the end product—but the kinetically slow nature of Co(II)/Co(III) redox conversion points to the likelihood of a less direct process, for example involving Fe(III) sites as mediators.

The EXAFS data at the cobalt K-edge show three strong peaks in its Fourier transform (Fig. 3b), which were fitted on the assumption that they represent progressive translation outward from Co in the [···Co–N≡C–Fe···] lattice. Features at approximate distances of 2, 3 and 5 Å thus represent Co–N, Co–C and Co–Fe distances, respectively [53].

The nearest neighbour distance Co–N is well defined and, initially, was fitted with a single parameter. The result, presented in Fig. 11a, is a progressive decrease in bond length as the Co site is oxidised. Simultaneously, the Debye-Waller factor goes through a maximum value at about +0.3 V, i.e., at partial conversion, with more typical (and similar) values for the film in its fully reduced (0.0 V) and fully oxidised (>0.7 V) states. Recalling the earlier discussion of the shapes of the raw spectra, enforcement of a single bond length is inconsistent with the application of a "molecular" model with distinct Co^{II} and Co^{III} sites of different geometry. If, as the raw data demand, one recognises the presence of two types of site, their existence must be included within the fitting regime.

Consider the situation at any given potential, at which a fraction x of Co species exist in the Co^{II} oxidation state, characterised by Co–N distance $R1$, and the remaining fraction $(1-x)$ of Co^{III} sites are characterised by Co–N distance $R2$; it is assumed that the structure of each species is independent of potential. The Debye-Waller factor represents a sum of thermal and static contributions to the total disorder. Potential variation leads to a changing distribution of Co^{II} and Co^{III}, so the potential variation in Debye-Waller factor has a structural (static) origin. In the event that the spectral features are unresolved, there will be a single broad feature at a mean value:

$$R = xR_1 + (1-x)R_2 \tag{3}$$

with an additional contribution σ^2_{st} to the total Debye-Waller factor, σ^2, of:

$$\begin{aligned}\sigma^2_{st} &= x(R_2-R)^2 + (1-x)(R_1-R)^2 \\ &= x(1-x)(R_1-R_2)^2\end{aligned} \tag{4}$$

Thus, the model predicts that a plot of σ^2 as a function of redox composition (represented by charge) will follow a parabolic curve, showing a maximum at x=0.5 (equal populations of the two redox forms) between the lower σ^2 values associated with the presence of the individual redox forms that dominate at potentials well above or below the redox transition.

The number of data points available clearly limits the precision, but the consistency of the qualitative behaviour with this model justifies a little further pursuit. Applying this model to the data, we find $R1 \cong 2.03$ (±0.02) Å and $R2 \cong$ 1.89 (±0.02) Å, so $(R1-R2)^2 \cong 200$ $(pm)^2$. σ^2_{st} peaks at x= 0.5, with a value of 50 $(pm)^2$. This is in good agreement with the fitted σ^2_{st} values if the vibrational contribution (represented by the single species at the end points) has the physically reasonable value of ca. 170 $(pm)^2$, and x=0.5 at $E \approx 0.3$ V. Furthermore, fitting the EXAFS data at E=0.3 V allowing distinct values for the first neighbour Co^{II}–N and

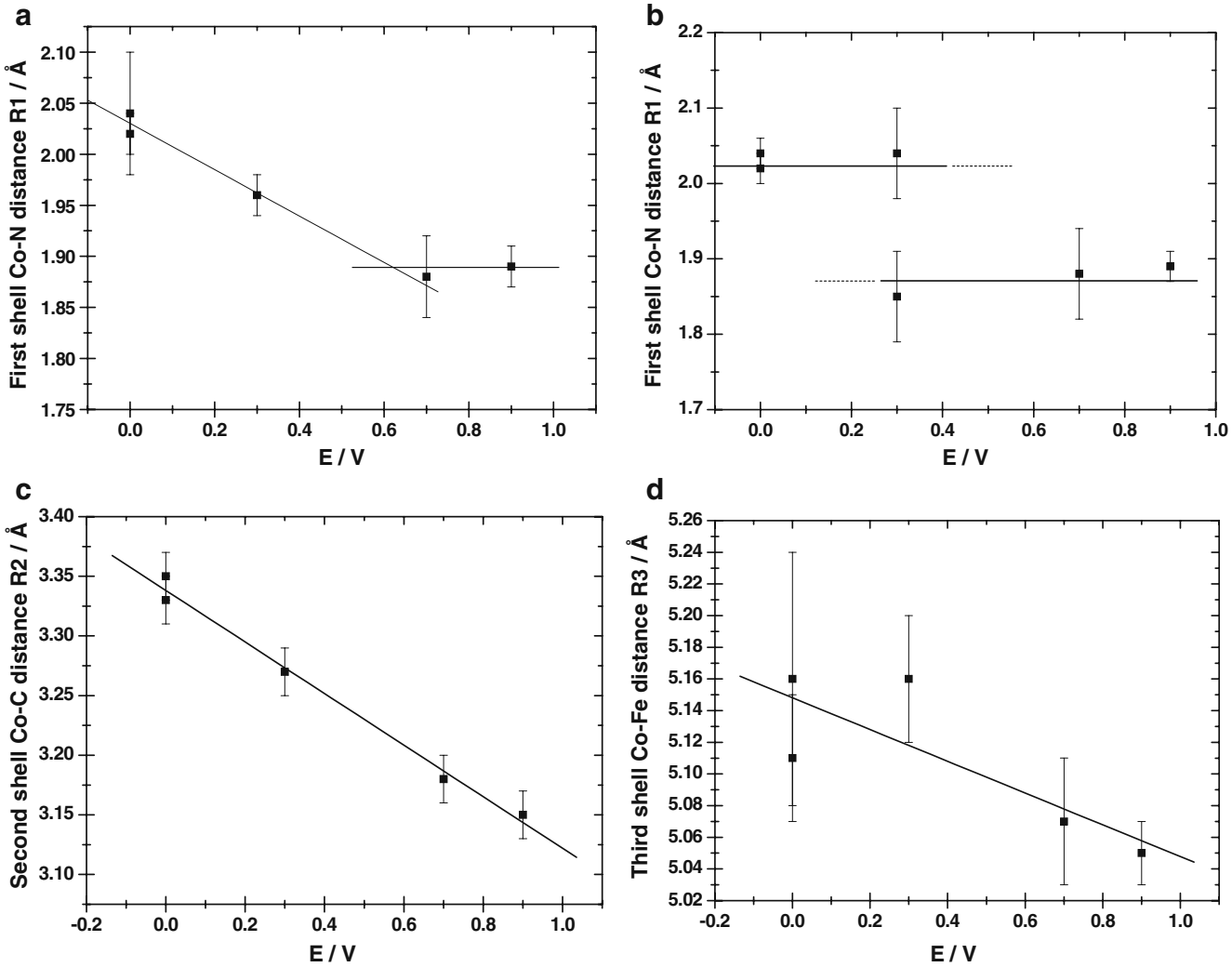

Fig. 11 Co K-edge EXAFS derived Co-neighbour atom distances in a cobalt hexacyanoferrate film as a function of potential. With the exception of (**b**), data are for a single shell fit and a linear fit of the data. Two values at the potential E=0.0 V denote replicate measurements on different instruments (stations 7.1 and 16.5). In each case, *lines* are a guide to the eye. **a** First shell Co–N distances. **b** First shell Co–N distances for split shell fit (see text). **c** Second shell Co–C distances. **d** Third shell Co–Fe distances

Co^{III}–N distances generates values for these distances (in the *mixed state* film, where $x \sim 0.5$) of 2.04 (±0.06) Å and 1.85 (±0.06) Å, respectively. These are in good agreement with the *single species* fits at the extremes of potential (where x=0 and 1), and the associated Debye-Waller σ^2 values are 150–200 $(pm)^2$. The outcomes for the split first shell Co–N distances are shown in Fig. 11b.

The presence of two distinct distances indicates that the cobalt hexacyanoferrate film behaves in a molecular manner, with discrete sites of integer oxidation state and *d* level occupancy. This contrasts with a solid state model, involving indistinguishable sites associated with delocalised charges in a partially filled *d*-band. The contrasting characteristics of these two models are worthy of brief discussion. In the molecular model, individual sites have charge and local structure associated with a given metal species. Potential does not influence the characteristics of these individual species, but rather their relative populations. In a thick film, of the type used here, electronic charge propagates by sequential self-exchange in a "hopping" mechanism, typically resulting in low conductivity [54]. In the solid-state model, there is a band structure with delocalised electrons not affiliated with any particular atom or bond. In this case, potential influences the (non-integer) charge and local structure of the metal ions in a continuous manner. To summarise, key features of the data that are consistent with the molecular model are a broad Co K-edge, the width of which changes with redox composition, and a characteristic Debye-Waller signature; these are inconsistent with the solid state model.

At the most positive potential (E=0.9 V) the fit gives an indication, albeit weak, of a Co–X distance of ca. 2.1 Å;

this is probably due to interstitial counterions (X = Co^{2+} or K^{+}; we cannot be specific) incorporated during deposition and/or cycling. The second (Co–C) and third (Co–Fe) shell distances decrease steadily with increasing film oxidation (see Fig. 11c and d). The low Debye-Waller factors obtained for these more distant coordination shells using only single scattering contributions suggest some multiple scattering, although inclusion of multiple scattering effects does not significantly improve the data fits. Nonetheless, this clearly shows that the [···Co–N≡C–Fe···] structure along the cube edge is not perfectly linear.

The difference between the Co–C and Co–N distances is independent of potential. Given the possibility of a non-linear structure, this difference (1.31 Å) will be a lower limit estimate of the C≡N bond length. Even this is somewhat longer than C≡N bonds typical of hexacyanometallate (ca. 1.15 Å), although other EXAFS studies [44] of this class of materials have revealed substantially longer C≡N distances.

The third shell distance is in a good agreement with (single crystal) crystallographic data for $Co_3(Fe(CN)_6)_2{\cdot}xH_2O$ [55]. The Fe site is a strong scatterer, so any additional contributions at this distance will be comparatively weak. Again, multiple scattering contributions are not significant. Comparing the Co–C and Co–Fe distances yields a lower limit (according to the extent of non-linearity of the [···Co–N≡C–Fe···] structure) for the Fe–C separation of 1.85–1.90 Å. As an internal consistency check, we note that this Co K-edge derived distance is in agreement with the value found by fitting Fe K-edge data.

X-ray photoelectron spectroscopy and infrared spectroscopy

It is clear even from the raw XPS data that Co and Ni hexacyanoferrate films respond quite differently upon voltammetric cycling. In the case of Co hexacyanoferrate films it is Fe that maintains constant oxidation state, with Co as the redox centre. This is unambiguously visible from the raw Co $2p_{3/2}$ XPS data (Fig. 7): there are clearly two components at BE=778.2 eV and BE=779.8 eV, attributable to Co^{II} and Co^{III}, respectively. Interestingly, although there are significant changes in the ratio of Co^{II} and Co^{III} species, both components (and thus species) are seen for samples emersed at both extremes of the potential range. We do not pursue this quantitatively or make comparisons with the Ni hexacyanoferrate system, given arguments based on sample vulnerability to atmospheric redox "contamination" during transfer. An interesting observation is the appearance at an emersion potential of 0.9 V of a small feature (at 707.3 eV) on the high binding energy side of the Fe $2p_{3/2}$ band, signalling oxidation of a small fraction of Fe^{II} to Fe^{III}.

The IR transmission data provide similar insights, but with the important distinction that these relate to the composition of the entire film. The ν(CN) bands are broad, consistent with mixed Co redox states. The vibrational frequency of the ν(CN) band changes from 2,100 cm^{-1} at E=0.0 V to 2,142 cm^{-1} at E=0.9 V and a small feature appears at 2,200 cm^{-1} at E=1.1 V. These vibrations can be assigned to films of (mixed) redox state $Fe^{II}Co^{II}$, $Fe^{II}Co^{II}Co^{III}$ and $Fe^{III}Fe^{II}Co^{III}Co^{II}$, respectively.

Turning to Ni hexacyanoferrate, emersion at E=0.0 V, results in a single narrow Fe 2p line at a binding energy of 705.5 eV, attributed to Fe^{II} centres. As the emersion potential is made more positive, a second Fe 2p appears at the higher binding energy of 707.1 eV (see Fig. 8); this is attributed to Fe^{III} centres. The areas under each of these features can be used to estimate the *surface* redox composition. At the negative extreme of the potential range (E=0.0 V), the fraction of *surface* sites in the reduced Fe^{II} state is ~100%; apparently, atmospheric oxygen does not oxidise the surface sites during transfer to the UHV chamber. At the positive extreme of potential (E=0.9 V), the majority (ca. 55%) of the Fe *surface* site population is in the Fe^{III} state, but this dominance is not overwhelming. For the Ni hexacyanoferrate film, no change was observed in the Ni $2p_{3/2}$ band: the shape and position (binding energy, BE=853.3 eV) remained at a value characteristic of Ni^{II} (see Fig. 8).

The IR data (see Fig. 10) for the ν(CN) mode in Ni hexacyanoferrate show a frequency change with film oxidation state: ν(CN)=2,106 cm^{-1} at E=0.0 V and ν(CN)=2,141 cm^{-1} at E=0.9 V. However, the bands are broad, indicating that not all the Fe centres are oxidised. This is interesting, in that the transmission IR measurement (which probes the bulk of the film) is not only consistent with, but also extends, the (surface sensitive) observation of partial oxidation by XPS.

Conclusions

Coordinated use of XAS (EXAFS and XANES), XPS and IR spectroscopies was used to extract redox compositional and structural information on films of electrodeposited Co and Ni hexacyanoferrates. In each case, electrochemistry was used to manipulate overall film redox state, although it cannot alone define the sources/sinks of electronic charge. For both systems, the techniques provide consistent pictures, although accessing information by distinct and independent routes. XPS-derived assays of metal ion oxidation state(s) relate to the outer *surface* of the film, while the XAS and IR methods (in the modes employed) sample the *bulk* (interior) of the film. Surprisingly, these two assays were generally not significantly different. In the

case of XAS and XPS, the responses relate directly to the metal species, while in the case of IR information on the metal species is inferred from changes in the behaviour of the adjacent cyanide ligands; it is gratifying that these direct and indirect probes yield consistent outcomes.

The XPS responses unequivocally show that the electrochemical response of Co hexacyanoferrate is associated with a formal $Co^{III/II}$ redox state change. The exception to this is a small amount of Fe^{II} oxidation at extremely positive potentials. Analogous data for Ni hexacyanoferrate unequivocally show that the electrochemical response of is associated with a formal $Fe^{III/II}$ redox state change. For both systems, edge shifts in XANES were consistent with the relevant XPS-derived conclusions.

Local structure around the metal atoms was extracted from EXAFS data in terms of M′–N, M′–C and M′–M″ distances and the associated Debye-Waller factors. Electroactive metal ion oxidation resulted in subtly different behaviours. In Co hexacyanoferrate, the Co-ligand distance shortened progressively and significantly with Co oxidation. In Ni hexacyanoferrate, the Fe-ligand distance did not shorten significantly with Fe oxidation.

In the Co hexacyanoferrate case, more detailed exploration of structure was possible. First, the contraction of the Co–N bond was associated with an essentially uniform "shrinkage", with the surrounding shells of C and Fe atoms moving inwards equally. As a consistency check, the estimates of Co–Fe distance measured outwards from either atom (via data at Co and Fe K-edges) were consistent. Second, the presence of static disorder (parameterized via the Debye-Waller factor) and its variation with redox state were consistent only with a molecular model involving discrete *d* levels and a mixture of distinct Co^{II} and Co^{III} sites; the data were not consistent with a solid state model.

Acknowledgements We thank Daresbury Laboratory for synchrotron beam time and Mr. R. Bilsborrow and Dr. Stephen Fiddy for technical support. MAS thanks Daresbury Laboratory and the Engineering and Physical Science Research Council for financial support.

We thank the NCESS Facility at Daresbury Laboratory for provision of XPS instrument time and Dr. Graham Beamson for helpful discussions.

References

1. Giorgetti M, Berrettoni M, Zamponi S, Kulesza PJ, Cox JA (2005) Electrochim Acta 51:511–516
2. Zamponi S, Giorgetti M, Berrettoni M, Kulesza PJ, Cox JA, Kijak AM (2005) Electrochim Acta 51:118–124
3. Kulesza PJ, Malik MA, Berrettoni M, Giorgetti M, Zamponi S, Schmidt R, Marassi R (1998) J Phys Chem B 102:1870–1876
4. Mardan A, Ajaz R, Mehmood A, Raza SM, Ghaffar A (1999) Sep Purif Technol 16:147–158
5. Hao X, Guo J, Liu S, Sun Y (2006) Trans Nonferr Met Soc China 16:556–561
6. Mimura H, Lehto J, Harjula R (1997) J Nucl Sci Technol 34:484–489
7. Kulesza PJ, Malik MA, Schmidt R, Smolińska A, Miecznikowski K, Zamponi S, Czerwiński A, Berrettoni M, Marassi RJ (2000) J Electroanal Chem 487:57–65
8. Eftekhari A (2004) Electroanalysis 16:1324–1329
9. Sato O, Hayami S, Einaga Y, Gu ZZ (2003) Bull Chem Soc Jpn 76:443–470
10. Yokoyama T, Ohta T, Sato O, Hashimoto K (1998) Phys Rev B 58:8257–8266
11. Sato O, Einaga Y, Iyoda T, Fujishima A, Hashimoto K (1997) Phys Chem B 101:3903–3905
12. Lezna RO, Romagnoli R, Tacconi NR, Rajeshwar K (2002) J Phys Chem B 106:3612–3621
13. Sato O, Einaga Y, Iyoda T, Fujishima A, Hashimoto K (1997) J Electrochem Soc 144:L11–L13
14. Sauter S, Wittstock G, Szargan R (2001) Phys Chem Chem Phys 3:562–569
15. Florescu M, Brett CMA (2004) Anal Lett 37:871–886
16. de Azevedo WM, de Mattos IL, Navarro M (2006) J Mater Sci: Mater Electron 17:367–371
17. Krylov AV, Lisdat F (2007) Electroanalysis 19:23–29
18. Florescu M, Barsan M, Pauliukaite R, Brett CMA (2007) Electroanalysis 19:220–226
19. Pauliukaite R, Hočevar SB, Hutton EA, Ogorevc B (2007) Electroanalysis 20:47–53
20. Prabakar SJR, Narayanan SS (2006) Anal Bioanal Chem 386:2107–2115
21. Yang M, Jiang J, Lu Y, He Y, Shen G, Yu R (2007) Biomaterials 28:3408–3417
22. Tung TS, Chen LC, Ho KC (2003) Solid State Ion 165:257–267
23. Jayalakshmi M, Scholz F (2000) J Power Source 91:217–223
24. Gómez-Romero P, Torres-Gómez G (2000) Adv Mater 12:1454–1456
25. Ambashta RD, Deshingkar DS, Wattal PK, Bahadur D (2006) J Radioanal Nucl Chem 270:585–592
26. Green-Pedersen H, Korshin GV (1999) Environ Sci Technol 33:2633–2637
27. Hg CW, Ding J, Gan LM (2001) J Solid State Chem 156:400–407
28. Martinez-Garcia R, Knobel M, Reguera E (2006) J Phys Condens Matter 18:11243–11254
29. Vaucher S, Fielden J, Li M, Dujardin E, Mann S (2002) Nano Lett 2:225–229
30. U.S. Patent, US 7,342,708 B2 Electrochromic Device Using Poly (3,4-Ethylenedioxythiopene) and Derivatives Thereof. Mar 11 2008
31. Giorgetti M, Berrettoni M, Filipponi A, Kulesza PJ, Marassi R (1997) Chem Phys Lett 275:108–112
32. Tang Q, Xiong W, Long L (2007) Anal Lett 40:1610–1621
33. Wang P, Yuan Y, Jing X, Zhu G (2001) Talanta 53:863–869
34. Bharati S, Nogami M, Ikeda S (2001) Langmuir 17:7468–7471
35. Joseph J, Gomathi H, Prahakara R (1991) J Electroanal Chem 304:63–269
36. Dostal A, Meyer B, Scholz F, Schroder U, Bond AM, Marken F, Shaw SJ (1995) J Phys Chem 99:2096–2103
37. Zakharchuk NF, Naumov N, Stosser R, Schroder U, Scholz F, Mehner H (1999) J Sol St Electrochem 3:264–276
38. Hermes M, Lovric M, Hartl M, Retter U, Scholz F (2001) J Electroanal Chem 501:193–204
39. Dostal A, Hermes M, Scholz F (1996) J Electroanal Chem 415:133–141
40. Schwudke D, Stosser R, Scholz F (2000) Electrochem Commun 2:301–306
41. Holmes SM, Girolami GS (1999) J Am Chem Soc 121:5593–5594
42. Verdaguer M, Girolami G (2004) In: Drillon M, Miller JS (ed) Magnetism: molecules to materials. Wiley, Weinheim

43. Gadet V, Mallah T, Castro I (1992) J Am Chem Soc 114:9213–9214
44. Hallmeier HK, Sauter S, Szargan R (2001) Inorg Chem Comm 4:153–156
45. Steen WA, Han SW, Yu Q, Gordon RA, Cross JO, Stern EA, Seidler GT, Jeerage KM, Schwartz DT (2002) Langmuir 18:7714–7721
46. Dent AJ, Mosselmans JFW (1995) An introduction to EXAFS data analysis. CCLRC Daresbury Laboratory, Warrington
47. Mosselmans JFW, A Guide to EXCURV98 http://srs.dl.ac.uk/XRS/Computing/Programs/excurv97/excurv98guide.htm Accessed 15 Nov 2009
48. Garcia-Jareno JJ, Navarro JJ, Roig AF, Scholl H, Vicente F (1995) Electrochim Acta 40:1113–1119
49. Siperko LM, Kuwana T (1983) J Electrochem Soc 130:396–402
50. Kaplun MM, Smirnov YE, Mikli V, Malev VV (2001) Russ J Electrochem 37:1065–1075
51. Bard AJ, Faulkner LR (2006) Electrochemical methods fundamentals and applications. Wiley, New York
52. Martinez-Garcia R, Knobel M, Balmaseda J, Yee-Madeira H, Reguera E (2007) J Phys Chem Sol 68:290–298
53. The Chemical Database Service, Daresbury Laboratory, UK http://cds.dl.ac.uk Accessed 25 Nov 2009
54. West AR (1984) Solid state chemistry and its applications. Wiley, Chichester
55. Juszczyk C, Hanson M, Ratuszna A, Malecki G (1994) J Phys Cond Matter 6:5697–5706